

Identification of fully coupled anisotropic plasticity and damage constitutive equations using a hybrid experimental–numerical methodology with various triaxialities

ZM Yue^{1,2}, C Soyarslan^{1,3}, H Badreddine², K Saanouni²
and AE Tekkaya¹

Abstract

A hybrid experimental–numerical methodology is presented for the parameter identification of a mixed nonlinear hardening anisotropic plasticity model fully coupled with isotropic ductile damage accounting for microcracks closure effects. In this study, three test materials are chosen: DPI000, CPI200, and AL7020. The experiments involve the tensile tests with smooth and notched specimens and two types of shear tests. The tensile tests with smooth specimens are conducted in different directions with respect to the rolling direction. This helps to determine the plastic anisotropy parameters of the material when the ductile damage is still negligible. Also, in-plane torsion tests with a single loading cycle are used to determine separately the isotropic and kinematic hardening parameters. Finally, tensile tests with notched specimens and Shouler and Allwood shear tests are used for the damage parameters identification. These are conducted until the final fracture with the triaxiality ratio η lying between 0 and $1/\sqrt{3}$ (i.e. $0 \leq \eta \leq 1/\sqrt{3}$). The classical force–displacement curves are chosen as the experimental responses. However, for the tensile test with notched specimens, the distribution of displacement components is measured using a full field measurement technique (ARAMIS system). These experimental results are directly used by the identification methodology in order to determine the “best” values of material parameters involved in the constitutive equations. The inverse identification methodology combines an optimization algorithm which is coded within MATLAB together with the finite element (FE) code ABAQUS/Explicit. After optimization, good agreement between experimental and numerically predicted results in terms of force–displacement curves is obtained for the three studied materials. Finally, the applicability and validity of the determined material parameters are proved with additional validation tests.

¹Institute of Forming Technology and Lightweight Construction, TU Dortmund, Germany

²ICD-LASMIS, University of Technology of Troyes, France

³Institute of Continuum and Material Mechanics, TU Hamburg-Harburg, Germany

Corresponding author:

ZM Yue, Institute of Forming Technology and Lightweight Construction, TU Dortmund, Germany.

Email: zhenming.yue@utt.fr

Keywords

Elastoplasticity, mixed hardening, ductile damage, microcracks closure, mechanical testing, parameter identification, inverse approach, Finite element method, anisotropy

Introduction

With increasing requirement of the crashworthiness and fuel efficiency, high strength steels and aluminum alloys are extensively used as body structure of modern automotive components. Due to the weak ductility of these materials, the prediction of their forming limits offers considerable challenges. Numerous failure criteria (based on necking or fracture) are proposed. Briefly speaking, methods for failure prediction in metallic materials can be classified in two groups: coupled and uncoupled damage approaches. In the case of uncoupled approaches, the damage effects on elastic and plastic strains are neglected and appropriate failure criteria are used to describe the material failure based on maximum or equivalent stress, maximum or equivalent strain, plastic work, plastic dissipation, and so on (Bai and Wierzbicki, 2008; Ebnoether and Mohr, 2013; Johnson and Cook, 1985; Rice and Tracey, 1969 among others). Due to their uncoupled nature, these models do not consider stress and stiffness decrease due to the damage-induced softening during deformation. Accordingly, they cannot accurately predict the localization and failure under various stress states.

In the case of coupled approaches, the effect of damage on the material behavior appears as mandatory in order to account for the damage-induced softening. In fact, taking into account the effect of ductile damage on the behavior of the deformed materials allows predicting the large inelastic strains and rotations of the processed workpieces and evolving boundary conditions. It can also indicate where and when the damaged zones appear and evolve during the forming process. From the microscopic viewpoint, ductile damage resulting from large plastic strains of metallic material develops in three main stages: (i) microvoids nucleation around the preexisting precipitates or second phases, (ii) microvoids growth, and (iii) microvoids coalescence leading to the initiation of macroscopically observed cracks. To account for the damage-behavior coupling, two approaches are widely used: the physically motivated approach initially developed by Gurson (1977) and the phenomenological approach based on continuum damage mechanics (CDM) (Lemaitre and Chaboche, 1985). Except the models by Gelin (1990) and Rousselier (1987), the former class of models involving Gurson approach and its extensions to various situations account only for the effect of the ductile damage on the stress decrease while keeping unchanged (i.e. insensitive to the damage occurrence) the material stiffness (Aravas, 1986; Benzerga and Leblond, 2010; Besson, 2009; Besson et al., 2003; Gologanu et al., 1995; Gurson, 1977; Needleman and Triantafyllidis, 1980; Onate and Kleiber, 1988; Pardoen et al., 2004; Rice and Tracey, 1969; Rousselier, 2001; Tvergaard, 1990 among many others).

The CDM approach follows the framework of thermodynamics of irreversible processes with state variables in which the damage is represented by a scalar (isotropic damage) or a tensor of various ranks (anisotropic damage) (Besson, 2010; Lemaitre, 1992; Lemaitre and Chaboche, 1985; Lemaitre et al., 2009; Lemaitre and Desmorat, 2005; Murakami, 2012; Saanouni, 2012; Voyiadjis and Kattan, 1992). The CDM approach has been extensively used to study different kinds of damage in various isotropic and anisotropic materials as can be found on the above cited books. Particularly, it has been widely used to describe the ductile damage of metallic materials under large plastic strains (Brokken et al., 1998; Celentano and Chaboche, 2007; Chow and Wang,

1987; Desmorat et al., 2007, 2010; Hartley et al., 1989; Lee et al., 1985; Saanouni and Chaboche, 2003; Saanouni and Hammi, 2000; Saanouni et al., 2011, 2008; Soyarslan and Tekkaya, 2010).

The model used in this study belongs to the class of CDM models. It accounts for the initial plastic anisotropy and mixed nonlinear isotropic and kinematic hardening fully coupled with ductile isotropic damage including the microcracks closure effects. In this model the triaxiality ratio, defined as the ratio between the hydrostatic stress (first stress invariant) and the equivalent stress (second stress invariant), is taken into account in the thermodynamic damage force Y when it is expressed in the stress space (Lemaitre, 1992). However, the third stress invariant involved in the Lode angle is not taken into account. In recent experimental studies, Bao and Wierzbicki (2004) showed that the Lode angle parameter also affects the damage evolution, especially at low stress triaxiality. Also Xue (2007) developed a damage plasticity model, which includes both the hydrostatic pressure and Lode angle influence. In Cao et al. (2013a) classical Lemaitre's damage model has been enhanced by introducing the Lode angle to describe the ductile damage evolution in Zirconium alloy. The Lode angle effect is out of the scope of the present paper and will be addressed in a forthcoming study. In fact, in a recent work of the authors (Badreddine et al., 2014) it has been shown that the effect of the Lode angle is automatically accounted for when anisotropic damage is used.

Each type of constitutive equations is characterized by a given number of material parameters which need to be determined based on appropriate experimental data. The determination of the values of these parameters for a given material is not an easy task. Various identification methodologies based on inverse approach have been proposed to identify different kinds of constitutive equations (Bonora, 1999; Bouchard et al., 2011; Cao et al., 2013a, 2013b; Eggertsen and Mattiasson, 2010; Khoddam et al., 1996; Yoshida et al., 1998, 2003). However, there is still no standard guideline which can help users to identify easily the overall involved material parameters. In the context of damage mechanics, most of the previous identification methodologies are proposed based on standard tensile tests. This cannot accurately capture the damage growth under more complex loading paths under changing triaxiality ratios. Bao and Wierzbicki (2004) carried out 15 tests of aluminum alloy to cover stress triaxiality ranging from $-1/3$ to 1, including uniaxial tension, notched specimens, specimens with a central hole, simple shear (SS) specimens, tensile tube, and cylindrical bars for upsetting tests. In order to obtain the threshold strain at different stress triaxialities, notched round bar and image processing methodology were used to calibrate the Gurson-Tvergaard-Needleman (GTN) model under multiaxial stress states (Bonora et al., 2005; Li et al., 2011; Yoshida and Ishikawa, 2011). A novel specimen geometry designed by Shouler and Allwood (2010), allowing proportional shear loading paths across the strain ratio ($-1 \leq (\varepsilon_2/\varepsilon_3) \leq 1/2$), can be performed using classical universal tensile machine. Another kind of shear specimen geometry, proposed by Merklein and Biasutti (2011) for performing forward and reverse SS tests, can be used to investigate the Bauschinger effect at room or high temperature. Note that, to avoid some difficulties related to the application of cyclic loading paths (Abel and Ham, 1966; Yoshida et al., 1998), Yin et al. (2012) proposed a modified twin bridge shear test. In the case of notched tension and shear tests, inhomogeneous stress and strain distributions are involved, and the stress-strain curves cannot be determined directly from the tests. The hybrid experimental-numerical methodology commonly called inverse method can be used for parameter identification. The inverse approach consists on minimizing the difference between available experimental data and numerically predicted results in order to find (iteratively) the best values of the overall material parameters (Bouchard et al., 2011; Khoddam et al., 1996; Yoshida et al., 1998, 2003).

The main goal of the present work is to introduce a methodology to guide the identification of the used fully coupled constitutive equations, which have 17 material parameters related to elasticity, anisotropic plasticity, and ductile isotropic damage. Various tests need to be conducted for the

identification of material parameters for three different materials, namely: DP1000, CP1200, and AL7020. Uniaxial tension tests (ASTM, 2000) can be performed in different loading directions with respect to the rolling direction (RD), which allow the identification of elastoplasticity parameters. The tests with cyclic loading paths can be used to determine the contribution of the kinematic hardening. For the ductile damage parameters, specimens with different geometries related to different triaxiality ratios need to be performed. The important microcracks closure effect parameter h has been taken into account, which dramatically decreases the rate of damage growth under compressive loading paths.

In the current study, the elastoplastic parameters and the damage parameters are identified separately. The elastoplasticity with the combined isotropic and kinematic hardening should be identified using uniaxial tensile tests and torsion tests with cyclic loading paths. Damage parameters can be determined with the help of the tensile tests with notched specimens and the SS tests, which can help to observe the formability of materials under different stress states with the triaxiality ratios η varying between 0 and $1/\sqrt{3}$. This identification procedure based on classical inverse approach is shortly described in Appendix 1. In the second chapter, the elastoplastic constitutive equations are briefly reviewed, which take into account the initial plastic anisotropy of Hill type and the mixed nonlinear isotropic and kinematic hardening fully coupled with ductile isotropic damage including the microcracks closure. This proposed model is already implemented into ABAQUS/Explicit FE code for the numerical simulation of sheet and/or bulk metal forming processes. It is also used here together with a MATLAB-based numerical inverse approach to determine the best values of the objective parameters. A complete experimental database is performed for the studied materials (DP1000, CP1200, and AL7020) using: uniaxial tension tests, notched tension specimens, twin bridge torsion test (Yin et al., 2012), newly proposed SS tests (Shouler and Allwood, 2010). A ARAMIS optical system distributed by the company GOM is also used to capture and record the strain distribution on the test zones, and the local force–displacement curves are plotted and used by the identification methodology. The validation of the identified model is performed using additional combined tension–shear tests.

Throughout this paper, the following notations will be used: $\underline{\underline{T}}$ and $\underline{\underline{T}}$ represent second-rank and fourth-rank tensors, respectively, $\underline{\underline{T}} : \underline{\underline{T}}$ and $\underline{\underline{T}} \otimes \underline{\underline{T}}$ denote the double contraction (or inner product) and tensor product, respectively. $\underline{\underline{T}}$ represents the effective state variable which is defined at the fictive undamaged configuration.

Outline of the fully coupled constitutive equations

The elastoplastic constitutive equations fully coupled with the isotropic ductile damage are developed in the framework of thermodynamics of irreversible processes with state variables assuming large plastic strains and small elastic strains. In order to ensure the required objectivity of the constitutive equations, the so-called rotating frame formulation is used which leads to the additive decomposition of the total strain rate tensor into an elastic small strain rate and a finite plastic strain rate (Badreddine et al., 2010; Saanouni and Chaboche, 2003). The detailed theoretical, numerical, and applicative aspects of various versions of the fully coupled formulations can be found in Saanouni (2012) and we limit ourselves here to giving the main feature of the particular model used in this study. The following couples of state variables are used: (i) $(\underline{\underline{\varepsilon}}^e, \underline{\underline{\sigma}})$ represents the elastoplastic flow; (ii) $(\underline{\underline{\alpha}}, \underline{\underline{X}})$ represents the kinematic hardening; (iii) (r, R) represents the isotropic hardening, and (iv) (d, Y) represents the isotropic ductile damage in Lemaitre and Chaboche (1985) sense. It should be noted that the damage variable takes values between 0 and 1 and the total fracture of the representative volume element (RVE) is achieved when $d = d_c = 1$. The strong

coupling between the plastic flow with hardening and the ductile damage is performed in the framework of total energy equivalence assumption (Badreddine et al., 2010; Saanouni, 2012; Saanouni and Chaboche, 2003), leading to the definition of the effective state variables $(\tilde{\underline{\varepsilon}}^e, \tilde{\underline{\sigma}})$, $(\tilde{\underline{\alpha}}, \tilde{\underline{X}})$, and (\tilde{r}, \tilde{R}) through the use of three damage-effect functions according to

$$\tilde{\underline{\varepsilon}}^e = g_e(d)\underline{\varepsilon}^e \quad \text{and} \quad \tilde{\underline{\sigma}} = \frac{\underline{\sigma}}{g_e(d)} \quad (1)$$

$$\tilde{\underline{\alpha}} = g_\alpha(d)\underline{\alpha} \quad \text{and} \quad \tilde{\underline{X}} = \frac{\underline{X}}{g_\alpha(d)} \quad (2)$$

$$\tilde{r} = g_r(d)r \quad \text{and} \quad \tilde{R} = \frac{R}{g_r(d)} \quad (3)$$

where the damage effect functions $g_e(d)$, $g_\alpha(d)$, and $g_r(d)$ are scalar valued, positive, and decreasing functions of damage with $g_e(d=0)=g_\alpha(d=0)=g_r(d=0)=1$ at the initial undamaged state and $g_e(d_c)=g_\alpha(d_c)=g_r(d_c)=0$ at the final fracture of the RVE. In this work the following choices of the damage effect functions are adopted

$$g_e(d) = g_\alpha(d) = \sqrt{1-d} \quad \text{and} \quad g_r(d) = \sqrt{1-d^\gamma} \quad (4)$$

where γ is a parameter governing the effect of ductile damage on the isotropic hardening compared to the kinematic hardening and elastic modules (Saanouni, 2012).

The microcracks closure phenomenon is generally observed for the loading paths alternating tension and compression phases. Indeed, if compression succeeds to tension with some microcracks created in tension, it is observed that these opened microcracks tend to close during the compressive phase of loading (see Lemaitre, 1992; Lemaitre and Desmorat, 2005; Saanouni, 2012 for more details). This leads to a partial or complete recovery of some damage-affected mechanical properties as the elastic modulus, hardening moduli, etc. and drastically reduces or even completely skips the damage evolution during the compression phase of the applied loading. This activation–deactivation of damage has been largely studied in the literature for various types of materials (Chaboche, 1992, 1993; Daudeville and Ladev  ze, 1993; Lemaitre, 1992; Lemaitre and Desmorat, 2005; Marigo, 1985; Ortiz, 1985; Saanouni, 2012; Simo and Ju, 1987; Zhu et al., 1992). The basic idea to account for this phenomenon is to decompose the tensorial state variables into negative and positive parts and to affect some material properties by the damage differently under positive and negative phases of the applied loading. This leads inherently to some theoretical problems directly related to the continuity and/or convexity loss of the yield function, state, and dissipation potentials (Chaboche, 1992, 1993; Li and Smith, 1998; Qi and Bertram, 1999).

In this work only the small elastic strain tensor (and inherently the associated Cauchy stress tensor) is decomposed into positive and negative parts leading to a damage release rate which is lower in compression than in tension. This allows having a lower damage rate in compression than in tension for the same amount of loading as can be found in Saanouni (2012). To do that, let us consider any symmetric second-rank tensor \underline{T} with $\underline{T}^{dev} = \underline{T} - (1/3)tr(\underline{T})\underline{1}$ its deviatoric part. The additive decomposition of this tensor into positive and negative parts $\underline{T} = \langle \underline{T} \rangle_+ + \langle \underline{T} \rangle_-$ can be made with $\langle \underline{T} \rangle_+ = \sum_{i=1}^3 \langle T_i \rangle \vec{e}_i \otimes \vec{e}_i$ and $\langle \underline{T} \rangle_- = \underline{T} - \langle \underline{T} \rangle_+$ where $\langle T_i \rangle$ is the i th eigenvalue of the tensor \underline{T} and \vec{e}_i its associated eigenvector. The notation $\langle x \rangle$ indicates the positive value of x , i.e. $\langle x \rangle = x$ if $x > 0$ and $\langle x \rangle = 0$ if $\langle x \rangle \leq 0$ and $\underline{1}$ denotes the unit second-rank tensor. Accordingly, the effect of the ductile

damage on the elastic behavior described by the effective variables of equation (1) is modified and decomposed into deviatoric and hydrostatic parts as following

$$t \left\{ \begin{array}{l} \tilde{\underline{\varepsilon}}^e = g_e(d) \langle \underline{\varepsilon}^e \rangle_+ + g_e(hd) \langle \underline{\varepsilon}^e \rangle_- \\ \quad = \sqrt{1-d} \left(\langle \underline{\varepsilon}^e \rangle_+ + \frac{1}{3} \langle tr(\underline{\varepsilon}^e) \rangle \underline{1} \right) + \sqrt{1-hd} \left(\langle \underline{\varepsilon}^e \rangle_- - \frac{1}{3} \langle -tr(\underline{\varepsilon}^e) \rangle \underline{1} \right) \\ \tilde{\underline{\sigma}} = \frac{\langle \underline{\sigma} \rangle_+}{g_e(d)} + \frac{\langle \underline{\sigma} \rangle_-}{g_e(hd)} \\ \quad = \frac{1}{\sqrt{1-d}} \left(\langle \underline{\sigma}^{dev} \rangle_+ + \frac{1}{3} \langle tr(\underline{\sigma}) \rangle \underline{1} \right) + \frac{1}{\sqrt{1-hd}} \left(\langle \underline{\sigma}^{dev} \rangle_- - \frac{1}{3} \langle -tr(\underline{\sigma}) \rangle \underline{1} \right) \end{array} \right. \quad (5)$$

in which $\underline{\varepsilon}^e$ stands for the deviatoric part of the small elastic strain tensor $\underline{\varepsilon}^e$ and the parameter $h \in [0.0 \ 1.0]$ is the microcracks closure parameter.

By using the effective strain-like variables defined above in the Helmholtz free energy taken as a state potential, the following state relationships can be easily obtained (Badreddine et al., 2010; Saanouni, 2012; Saanouni et al., 1994)

$$\underline{\sigma} = 2\mu_e \left[(1-d) \langle \underline{\varepsilon}^e \rangle_+ + (1-hd) \langle \underline{\varepsilon}^e \rangle_- \right] + k_e \left[(1-d) \langle tr(\underline{\varepsilon}^e) \rangle - (1-hd) \langle -tr(\underline{\varepsilon}^e) \rangle \right] \underline{1} \quad (6)$$

$$\underline{X} = (1-d)^{\frac{2}{3}} C \underline{\alpha} \quad (7)$$

$$R = (1-d^r) Q r \quad (8)$$

$$Y = Y^e + Y^\alpha + Y^r \quad (9)$$

$$Y^e = 2\mu_e \left[\langle \underline{\varepsilon}^e \rangle_+ : \langle \underline{\varepsilon}^e \rangle_+ + h \langle \underline{\varepsilon}^e \rangle_- : \langle \underline{\varepsilon}^e \rangle_- \right] + k_e \left[\langle tr(\underline{\varepsilon}^e) \rangle^2 + h \langle -tr(\underline{\varepsilon}^e) \rangle^2 \right] \quad (10)$$

$$Y^\alpha = \frac{1}{3} C \underline{\alpha} : \underline{\alpha} \quad (11)$$

$$Y^r = \frac{1}{2} \gamma d^{r-1} Q r^2 \quad (12)$$

where μ_e and λ_e are the classical Lamé's constants and $k_e = (2\mu_e + 3\lambda_e)/3$ is the compressibility modulus, while the parameters C and Q are the kinematic and the isotropic hardening moduli, respectively. Clearly, equation (10) shows that the microcracks closure parameter h serves to reduce the damage force for compressive load if $h < 1$ and if $h = 0$ there is no more contribution of the compressive load on the damage force. This is the simplest way to differentiate the damage rate under tension and compression.

Note that the use of the total energy release rate given by equations (9) to (12) in the damage evolution (see equation (18)) leads to a contribution of the elastic as well as the hardening parts in the damage growth. It is important to highlight that the microcracks closure effect is only applied to the elastic part of the damage energy release rate (equation (10)). In Figure 1 the microcracks closure effect on the ductility, here given as the equivalent plastic strain at fracture, comparing both elastic and total energy in the damage evolution is depicted. This figure describes the evolution of the ductility (i.e. equivalent plastic strain before final failure $d=0.9$) with respect to the triaxiality. As

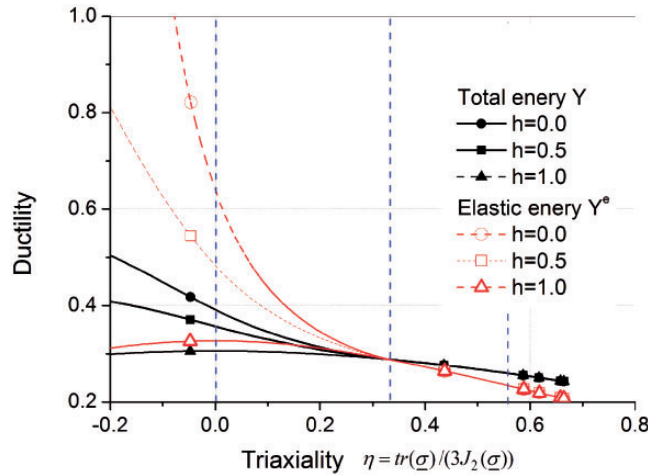


Figure 1. Effect of microcracks closure parameter h on the plastic equivalent strain at final rupture ($d = 0.9$) as a function of the triaxiality ratio.

shown in this figure, the ductility increases for negative triaxiality when $h < 1$, i.e. when the microcracks closure effect is accounted for. As anticipated, this increase is relatively more important when considering only the elastic part of the damage energy release rate, for which it is observed that the ductility tends to infinity for the triaxiality values below $-1/3$, i.e. uniaxial compression, for the case $h = 0$. While the existence of cut-off triaxiality for fracture is an active research field, the mathematical flexibility of the current model can account for damage development for the studied triaxiality range. Note that in the original Lemaitre's damage model, which uses only the elastic part of the energy release rate as the damage driving force, $h = 0.2$ is suggested for metallic materials.

To ensure the thermodynamic admissibility of the model, the stress-like variables being defined by equations (6) to (12) and the associated flux variables (\underline{D}^p , $\underline{\dot{\alpha}}$, \dot{r} , and \dot{d}) should be defined in such a manner that the Clausius–Duhem inequality $\Phi = \underline{\sigma} : \underline{D}^p - \underline{X} : \underline{\dot{\alpha}} - R\dot{r} + Y : \dot{d} \geq 0$ (\underline{D}^p being the plastic strain rate) is identically satisfied. To achieve this goal, we introduce in the framework of nonassociative plasticity a yield function f^p and a plastic potential F^p (Badreddine et al., 2010), both positive and convex functions of their main arguments in the stress space. From these functions, the evolution equations are obtained through the normality rule. In this study, a single surface model is used to describe the damaged elastoplastic behavior using the same yield function and plastic potential chosen as

$$f^p = \frac{\|\underline{\sigma} - \underline{X}\|}{\sqrt{1-d}} - \frac{R}{\sqrt{1-d^v}} - \sigma_y = 0 \quad (13)$$

$$F^p = \frac{\|\underline{\sigma} - \underline{X}\|}{\sqrt{1-d}} - \frac{R}{\sqrt{1-d^v}} + \frac{3a}{4(1-d)C} \underline{X} : \underline{X} + \frac{b}{2(1-d)Q} R^2 + \frac{S}{s+1} \left(\frac{Y - Y_0}{S} \right)^{s+1} \frac{1}{(1-d)^\beta} \quad (14)$$

With $\|\underline{\sigma} - \underline{X}\| = \sqrt{(\underline{\sigma} - \underline{X}) : \underline{H} : (\underline{\sigma} - \underline{X})}$ is the anisotropic Hill48 equivalent stress characterized by an anisotropic operator \underline{H} having six anisotropic parameters F , G , H , L , M , and N and σ_y is the initial yield stress. Applying the well-known normality rule leads to the following flux variables

which define the evolution of the dissipative phenomena (Badreddine et al., 2010; Saanouni, 2012; Saanouni et al., 1994)

$$\underline{D}^p = \dot{\lambda} \frac{\partial f^p}{\partial \underline{\sigma}} = \frac{\dot{\lambda}}{\sqrt{1-d}} \frac{\underline{H} : (\underline{\sigma} - \underline{X})}{\|\underline{\sigma} - \underline{X}\|} = \frac{\dot{\lambda}}{\sqrt{1-d}} \tilde{n} \text{ with } \tilde{n} = \frac{\underline{H} : (\underline{\sigma} - \underline{X})}{\|\underline{\sigma} - \underline{X}\|} \quad (15)$$

$$\dot{\underline{\alpha}} = -\dot{\lambda} \frac{\partial F^p}{\partial \underline{X}} = \frac{\dot{\lambda}}{\sqrt{1-d}} (\tilde{n} - a\tilde{\alpha}) \quad (16)$$

$$\dot{r} = -\dot{\lambda} \frac{\partial F^p}{\partial R} = \dot{\lambda} \left(\frac{1}{\sqrt{1-d}} - br \right) \quad (17)$$

$$\dot{d} = \dot{\lambda} \frac{\partial F^p}{\partial Y} = \frac{\dot{\lambda}}{(1-d)^\beta} \left(\frac{\langle Y - Y_0 \rangle}{S} \right)^s \quad (18)$$

where a and b characterize the nonlinearity of the kinematic and isotropic hardening, respectively, and S , s , β , and Y_0 are the material parameters defining the ductile damage evolution. The plastic multiplier $\dot{\lambda}$ can be determined from the consistency condition $\dot{f}^p = 0$. If $f^p = 0$, however it will be kept as the main unknown at each integration point of each finite element which will be determined from the FE calculation.

This model is implemented into ABAQUS/Explicit© finite element code through the VUMAT user routine. This subroutine is developed using a purely implicit numerical iterative integration algorithm based on the well-known elastic prediction–plastic correction method (Badreddine et al., 2010; Saanouni, 2012; Saanouni and Chaboche, 2003).


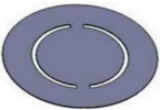


Application to three metallic materials

Experimental setup

In this study, three 1.5 mm thickness sheet metals, namely DP1000, CP1200, and AL7020, which are widely used in automotive industry, are investigated in order to test the reliability of the proposed identification methodology. For this purpose, adequate experiments, summarized in Table 1, need to be performed for the identification of the overall material parameters of the proposed model. The tensile load versus global displacement curve in uniaxial tensile tests (UT, Figure 2(a)) as well as the torsion angle versus the torsion torque curve in the two bridge torsion tests (TBT, Figure 2(b)) has been used for the identification of elastoplastic parameters.

For the determination of the damage parameters, prenotched tensile tests (PNT, Figure 3(a)) and SS tests (Figure 3(b)) are performed until final fracture to observe the ductile damage development under different loading paths characterized by various triaxiality ratios. With ARAMIS system, 1.0 and 4.0 mm away from the central line of cutting section on PNT specimens are chosen as the reference coordinates for local displacement output. Local displacement versus global force of PNT is chosen as experimental output for the (S, s, β, Y_0) determination, and global displacement versus global force of SS can test the damage evolution in shear stress state for microcracks closure h determination. A constant displacement rate of 0.1 mm/s is performed to insure the quasi-static deformation state.

Table 1. Experimental specimens and their association to material parameters.

	Test Design	Parameters	Number of parameters	Methodology
Elastoplasticity	UT 	$E, \nu, \sigma_y, F, G, H, L, M, N$	9	Analytical
	TBT 	C, a, Q, b	4	Inverse
Damage	PNT 	S, s, β, Y_0	4	Inverse
	SS 	h	1	Inverse

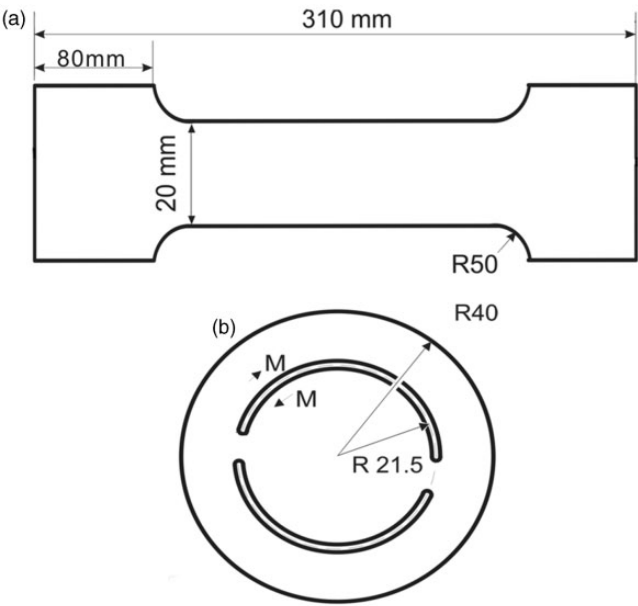


Figure 2. Specimen geometries for determination of plasticity parameters (a) UT, (b) TBT.

Firstly, the material parameters related to the plastic behavior without damage are determined. The elasticity parameters (E, ν) are determined from UT with analytical approach. The plastic flow parameters ($\sigma_y, F, G, H, L, M, N, C, a, Q, b$) are determined from UT and TBT tests. To cover the anisotropic behavior of materials, the UT specimens are prepared in three directions according to

the RD $0^\circ, 45^\circ, 90^\circ$. The planar anisotropy parameters ($F, G, H, N, M = 1.5, L = 1.5$) are calculated using anisotropy ratios r_0, r_{45}, r_{90} , respectively

$$F = \frac{H}{r_{90}}; \quad G = \frac{H}{r_0}; \quad G + H = 1; \quad 2 \cdot r_{45}(F + G) = 2 \cdot N - F - G \quad (19)$$

The detailed design of TBT tests can be found in Yin et al. (2012). The data outputs in the form of cyclic torsion angle–moment curves are monitored directly from the testing machine and used to isolate the kinematic hardening parameters (X, α).

Secondly, the material parameters relative to the damage variable (S, s, β, Y_0, γ) are determined from PNT tests. With the increase of notch radius, the damage evolution under different states of tension stress can be obtained corresponding to various triaxiality ratios (theoretically between uniaxial tension $\eta = 1/3$ and plane strain tension $\eta = 1/\sqrt{3}$). The test zones of PNT specimens (see Figure 3(a)) are constructed with two arcs whose horizontal length is 10 mm with three notched radius 5, 10, and 20 mm. Local displacement got with ARAMIS optical measurement device and global force curves are used as the experimental response.

For the sake of determination of the microcracks closure parameter h , SS is proposed corresponding to triaxiality ratio $\eta = 0.0$ (theoretically). The SS specimens (see Figure 3(b)) have double test zones which can efficiently avoid the torque caused by the load imbalance on each test zone (Shouler and Allwood, 2010). From the zoom of Figure 3(b), when q equals to zero, SS stress state is obtained in the critical zone. When q value is 1.25 and 2.5 mm, and while keeping the connection band to be constant, a combined tension and shear stress state is created. These two geometries will be used for the validation of the identified parameters. Considering the unpredictable position of

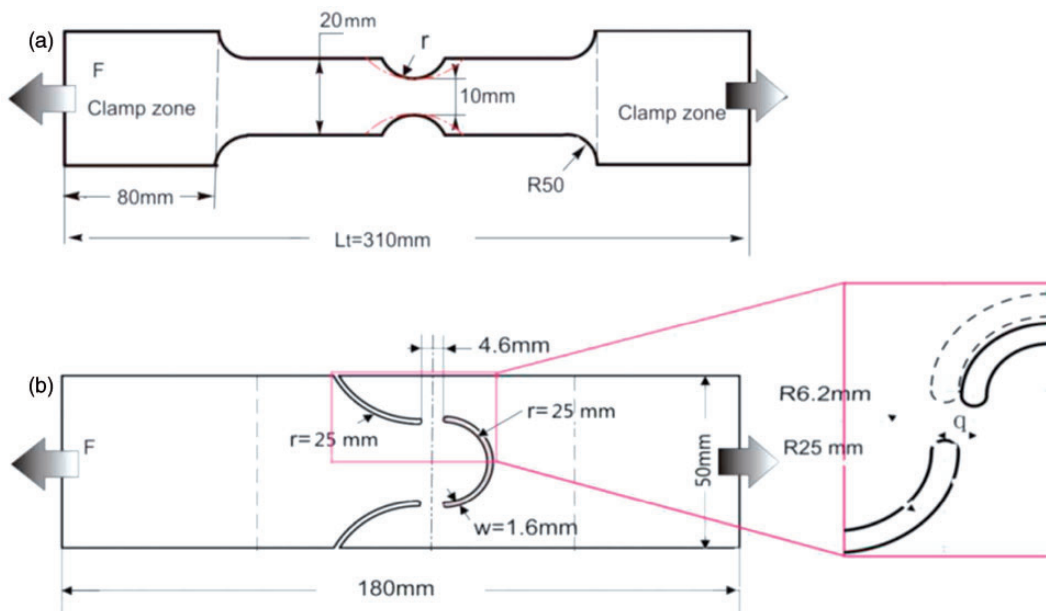


Figure 3. Specimen geometries for determination of damage parameters: (a) PNT, (b) SS.

onset fracture, ARAMIS device is not used here, and the global displacement–force curves are used as experimental response in these tests.

The digital image analysis system ARAMIS used in PNT tests is one among the very efficient tools to capture the displacement and strain distribution on the specimen surface, which works by tracking the gray value pattern in small neighborhood during deformation. Figure 4 shows an example of data dealing process in the tests. The digital system can accurately record the coordinates of each point on the captured pictures. The frequency of the picture acquisition is set to be 5 Hz, and pixel size is set to be 0.2 mm in this study. Due to the loss of speckle pattern of the paint on the specimen boundaries, it is not possible to accurately keep track of evolution of the curvature at the edges with deformation. The pixel points on the central line following loading direction, 1.0 and 4.0 mm ($X_1 = 2$ and 8 mm, as shown in Figure 4) away from the central line of the cutting section are chosen as the reference coordinates.

Identification of the fully coupled model

Inverse methodology scheme. As presented in Table 1, in order to determine separately the kinematic hardening (parameters C , a) and isotropic hardening (parameters Q , b) as well as the ductile damage parameters (S , s , β , Y_0) and the microcracks closure (parameter h), an inverse methodology is used. This method enables the usage of unusual test setups or even the forming process itself (Gelin and Ghouati, 1994; Unger et al., 2008) since the assumption of homogeneous deformation field is not needed anymore. In this study, for the kinematic hardening parameters (C , a), the measured moments versus rotation angles obtained from TBT tests are used. In order to form the objective function, the experimental and numerical curves having different discretizations will be

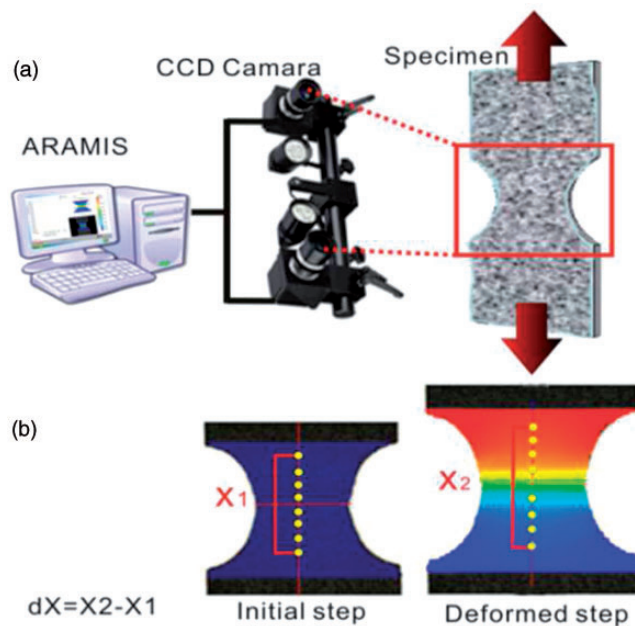


Figure 4. Referred point output methodology with ARAMIS measurement system.

linearly interpolated at the same rotation angle values. Fifty integration intervals are used for forward and backward steps, adding up to 100 data points for one loading cycle. There are the same weighting between the forward and backward curves. The similar scheme is used to determine S , s , β , Y_0 with local node distance versus global force from PNT tests and also determine the h with the global distance versus the global force from SS tests.

The identification methodology combines, thanks to Python script, the ABAQUS FE software with the MATLAB-based minimization code by reading the input files, comparing the output results with the experimental measurements, builds and minimizes the objective function, and deliver the best set of the material parameters which minimizes the difference between the numerically predicted and the experimental results (see Appendix 1).

Elastoplastic parameters' identification. The determined elastoplastic parameters are presented in Table 2. From UT tests, the elasticity parameters (E, ν) and initial yield stress σ_y can be obtained directly, and with the Lankford parameters r in three directions (Figure 5(a)) and equation (19), the anisotropic parameters of Hill 48 can be determined with this analytical approach. The combined hardening parameters are determined with the TBT experimental response and simulation responses. Without the damage coupled, the simulations are conducted with ABAQUS/Explicit using user's subroutine VUMAT and compared with experimental response before the maximum value of the load.

Table 2. Elastoplastic parameters obtained from UT and TBT specimens.

	E (GPa)	ν	σ_y (MPa)	Q (MPa)	b	C (MPa)	a	F	G	H	L	M	N
DPI1000	208.0	0.3	809.0	4000.0	13.0	32,000.0	150.0	0.525	0.546	0.455	1.5	1.5	1.67
CP1200	207.0	0.3	980.0	5848.0	37.0	37,000.0	507.0	0.567	0.610	0.389	1.5	1.5	1.37
AL7020	69.8	0.3	322.0	675.0	8.0	2260.0	75.0	0.631	0.634	0.366	1.5	1.5	1.4

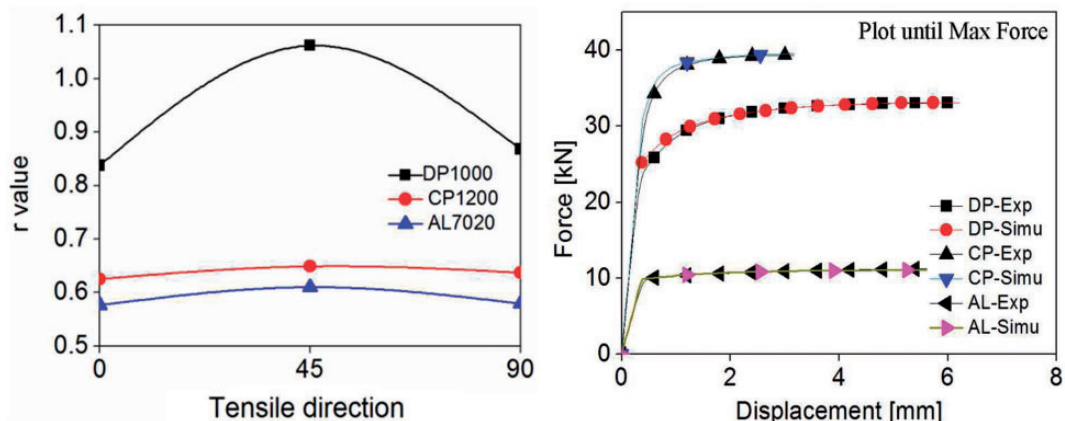


Figure 5. (a) The r -value in direction respect to rolling directions, (b) force–displacement curves for uniaxial tension.

Normally, the damage just affects the degeneration process of deformation after the maximum load. For the explicit simulation of the quasi-static deformation process, kinetic energy should be controlled less than 10% of the internal energy, so the kinetic energy can maintain a minor value compared with whole internal energy, and the inertia effects can be neglected, so the quasi-static process is ensured according to the energy conservation principle. The displacement rate is 10 mm/s, and the time increment is fixed to be 2×10^{-6} with mass scaling method.

Figure 5(b) shows the comparison of experimental–numerical responses in monotonic loading condition in the forms of force–displacement curves before the maximum force value, which can prove the accuracy of determined parameters in unique loading condition.

Figure 6 shows the results obtained for the three materials when subject to one loading cycle in torsion (loading–unloading). With the same prestrain 0.6 degree of torsion for DP1000 (Figure 6(a)) and CP1200 (Figure 6(b)), the CP1200 presents less Bauschinger effect and its saturation value is $0.07\sigma_y$, for kinematic hardening can satisfy the requirement, compared to $0.26\sigma_y$ for DP1000. With prestrain 1.5 degrees of torsion for AL7020 (Figure 6(c)) the saturation value is $0.1\sigma_y$, the Bauschinger effect in inverse direction can be obtained using the determined hardening parameters.

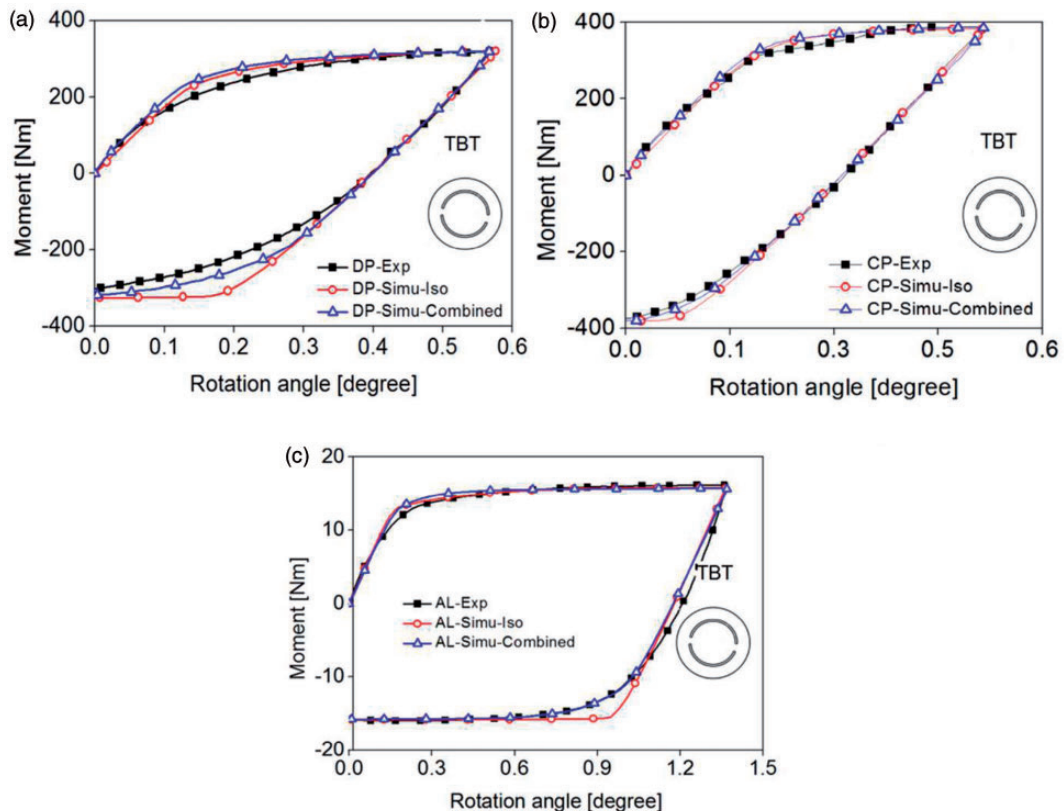


Figure 6. Numerical and experimental moment–angle curve comparison using the TBT test loading in rolling direction of plate with identified kinematic hardening parameters: (a) DP in shear loading, (b) CP in shear loading, (c) AL in shear loading.

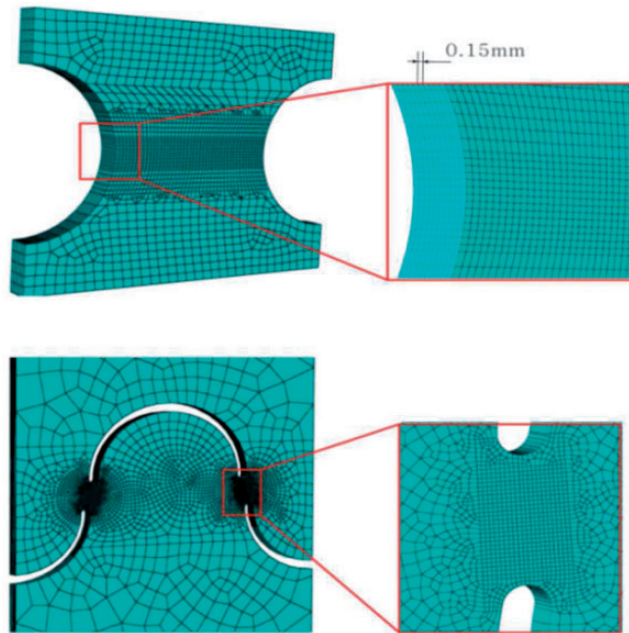


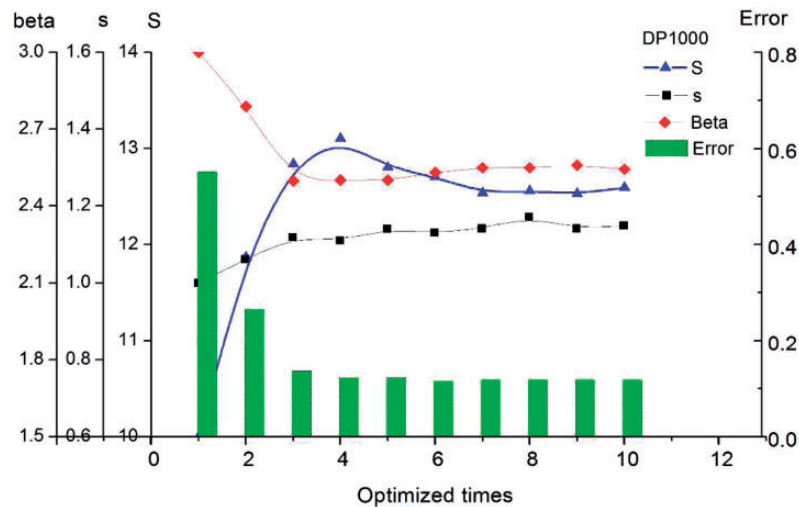
Figure 7. Design FEM mesh: (a) notched specimen, (b) shear specimen.

Damage parameters' identification. With the elastoplasticity parameters determined earlier, the PNT and SS are simulated with the same setting conditions in ABAQUS as used above. Since the present model is fully local and accounts for damage-induced softening, the influence of mesh size on damage evolution is handled via accounting mesh size as a process parameter as well. A finer mesh will lead to a faster damage evolution meaning that the numerical solution depends on the mesh size. In fact, the straightforward way to ensure the mesh independency is to use appropriate nonlocal formulation as widely discussed in the literature (see for example the recent book by Saanouni (2012)). Accordingly, a constant minimum mesh size of 0.15 mm on the plate surface and in thickness direction is used in the critical deformation zone where the fracture is expected. Figure 7 shows an example of the mesh conditions for PNT and SS specimens.

The numerical responses of PNT tests (global forces over local info-node displacements) are used into the optimization program to compare with the experimental responses. For the inverse optimization methodology, the initial values of input damage parameters and normalization method have strong influence on the convergence of the objective function (more detail presented in Appendix 1). In order to minimize the objective function, the trust region reflective method is used. The experimental responses have the linearly interpolated displacements of the local nodes with equal weighting. The optimization process involves the approximate solution of a large linear system based on the method of preconditioned conjugate gradients. For the time consuming, the first guessed input damage parameters can be determined first with local method and then taken into the optimization program. The critical damage value is fixed to be 0.99 in order to capture the full process of material degeneration behavior, and γ here is fixed to be 4.0. Y_0 is the threshold damage potential value where the bifurcation happens between experimental response and numerical response without damage effect. The contribution of any other damage parameter to damage

Table 3. Damage parameters obtained from PNT and SS tests.

	S (MPa)	s	β	γ_0 (MPa)	H
DPI000	12.5	1.15	2.5	2.0	0.25
CPI200	10.2	1.31	1.98	2.0	0.21
AL7020	4.50	1.48	3.4	0.0	0.3

**Figure 8.** Convergence of damage parameters of DPI000 during the iterative process.

evolution is not the same, so the influence of each damage parameter (S, s, β) should be well understood, which has been well described in Saanouni (2012).

By minimizing the error of the objective function of each test simulation with the nonlinear least squares method, an optimum solution of damage parameters for different geometries is obtained at last. The optimal results are presented in Table 3, and Figure 8 shows convergence of damage parameters (S, s, β) of DPI000 during the iterative process.

Figure 9 shows the results of PNT tests in terms of force–displacement curves for each measurement point using ARAMIS. Three figures cover three different notched radii, Figure 9(a) for 5.0 mm, Figure 9(b) for 10.0 mm, and Figure 9(c) for 20.0 mm, and for each simulation the nodes 1.0 and 4.0 mm away from the central axis in the notch section are shown, which represent different displacement fields on the critical deformation zone. It can be found there is a little discrepancy of the maximum loadings between experimental and numerical responses shown in Figure 9(a) and Figure 9(b). This discrepancy can be explained by the change of the stress states, and there are less regards on the effect of stress states on yield surfaces in our model. In Figure 10 which shows the result comparisons of SS tests, each figure includes the diagrams of loading over displacement. With the addition of h , the limit deformation is enlarged, as shown in Figure 10(a).

Good agreement of the beginning part of the loading curves between experimental and numerical responses (Figures 9 and 10) shows a good determination of the elastoplastic parameters.

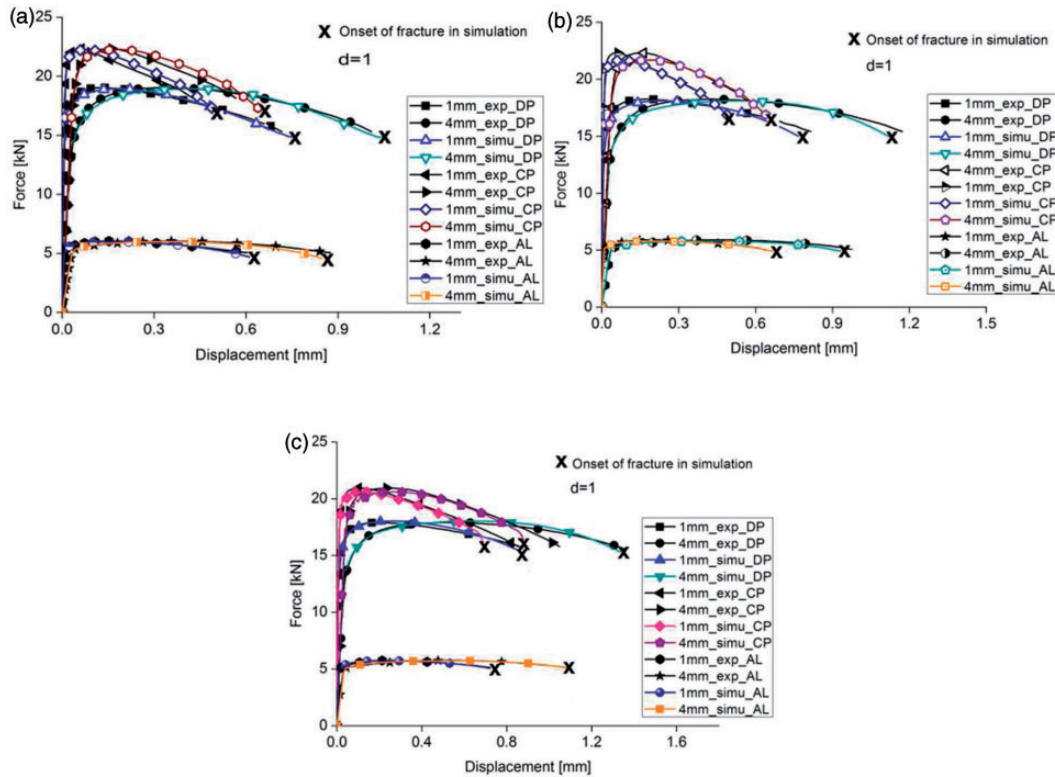


Figure 9. Numerical and experimental responses comparison of PNT tests (the symbol “X” indicates the first fully damaged integration point in the specimen): (a) radius 5.0 mm, (b) radius 10.0 mm, (c) radius 20.0 mm.

The degeneration process of the simulation strongly relates to the damage parameters. The simulation results well demonstrate the behavior of the sheets in degeneration process in PNT and SS tests. Figure 10 also shows the comparisons of experimental responses and numerical responses for SS tests in two cases: coupled damage and uncoupled damage with the same model parameters, which can clearly show the damage contribution during the forming. All these results prove the applicability of this methodology. The model parameters determined above are validated using SS tests (Figure 3(b)) with $q=1.25$ and 2.5 mm (shown in “**Validation using additional tests**” section).

Analysis of the damage effect. With the optimized parameters, the contours of the crack surface of PNT for AL7020 are shown in Figure 11, the notched radius is 5 mm. A constant minimum mesh size of 0.15 mm on the plate surface and in thickness direction is used in the critical deformation zone where the fracture is expected. During the whole forming process, when $d=1$, the element will fail and be deleted from mesh (kill-element technique). The initial failure element locates in the center of notched zone, and finally extends to the edge of the specimen, that can be explained by the relationship of triaxiality ratio and equivalent limit plastic strain. Normally in tension states, with increase of triaxiality ratio, the equivalent limit plastic strain will decrease, in notched tension tests, the η value in the center is higher than the value on the edge, and also the middle thickness of the

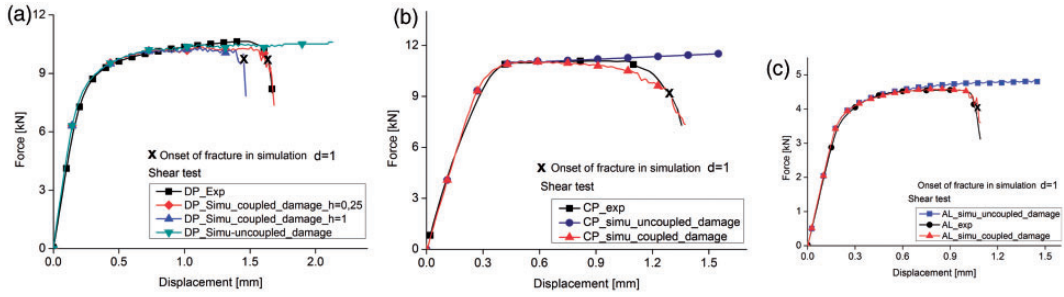


Figure 10. Numerical and experimental responses comparison of SS tests.

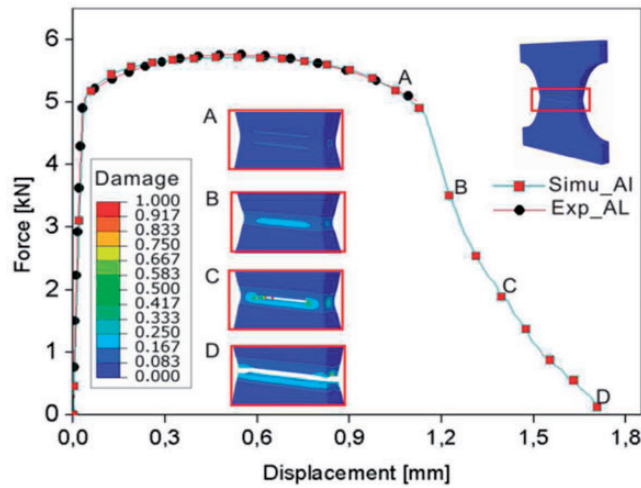


Figure 11. Crack initiation and propagation at the notch region regarding its location on the force–displacement curve.

section indicates to be thinner than the outside part. And also for the specimens with different radii, the η value changes in the critical zones. Considering the different radii in our tests (5.0, 10.0, 20.0 mm), the triaxiality ratio should be $\eta_5 > \eta_{10} > \eta_{20}$, and further the limit equivalent strains should be $\bar{\epsilon}_5^{eq} < \bar{\epsilon}_{10}^{eq} < \bar{\epsilon}_{20}^{eq}$, which corresponding to deformation behaviors of different geometry in Figure 9.

The relationship between equivalent plastic strain and stress triaxiality ratio at the critical point is shown in Figure 12. During the whole process, the flow tendencies of triaxiality ratios development at the critical and central point of the specimens are indicated to be different. For the central point of SS, it shows a constant waving near the 0.1 value, while the value of critical point increases with the deformation. For PNT, it is found that with the increase of notched radius, the triaxiality ratio decreases, and the equivalent plastic strain increases. The triaxiality ratio actually affects the deformation capability of the sheet.

Comparison between plane stress and three-dimensional (3D) solid. Besides the brick element (C3D8R, 3D), PNT and SS tests are also simulated with CPS4R (2D) element. In Figure 13, one

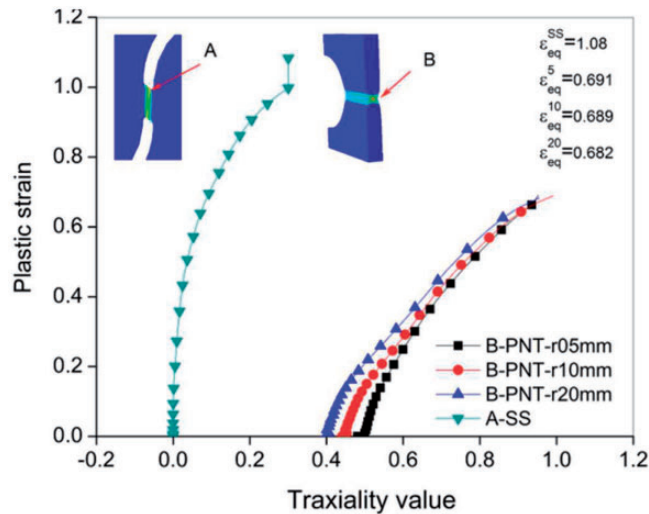


Figure 12. Evolution of the equivalent plastic strain as a function of triaxiality ratio until fracture for the critical point for SS and PNT tests.

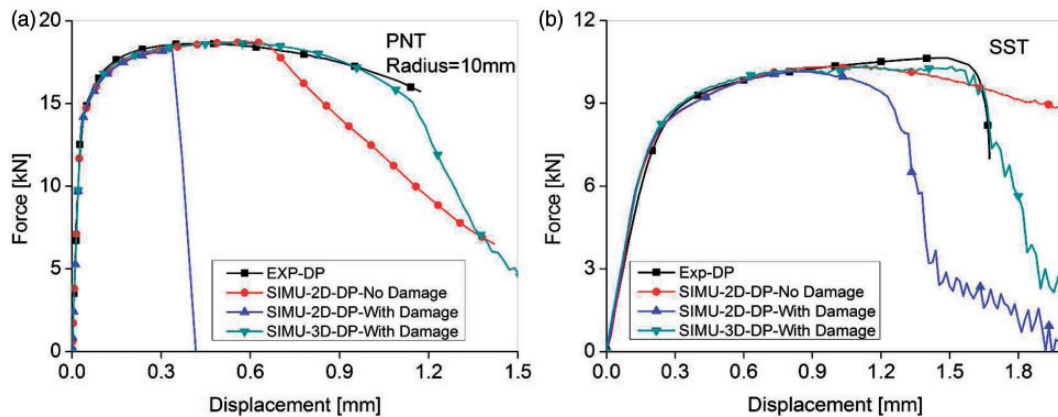


Figure 13. Numerical and experimental responses comparison: (a) PNT simulation with 2D and 3D brick element, (b) SS simulation with 2D and 3D brick element.

comparison of PNT and SS simulations is made with two different elements. Due to the less capability against necking or localization (the stress in the thickness direction is assumed to be zero), CPS4R element is difficult to represent the behavior of the sheet after the maximum loading point even without damage. With the same damage parameters, the damage initiation occurs earlier with two-dimensional elements. The results of SS test are shown to be more reasonable compared to PNT test which can be explained by the less localization in the critical zone during the shear deformation.

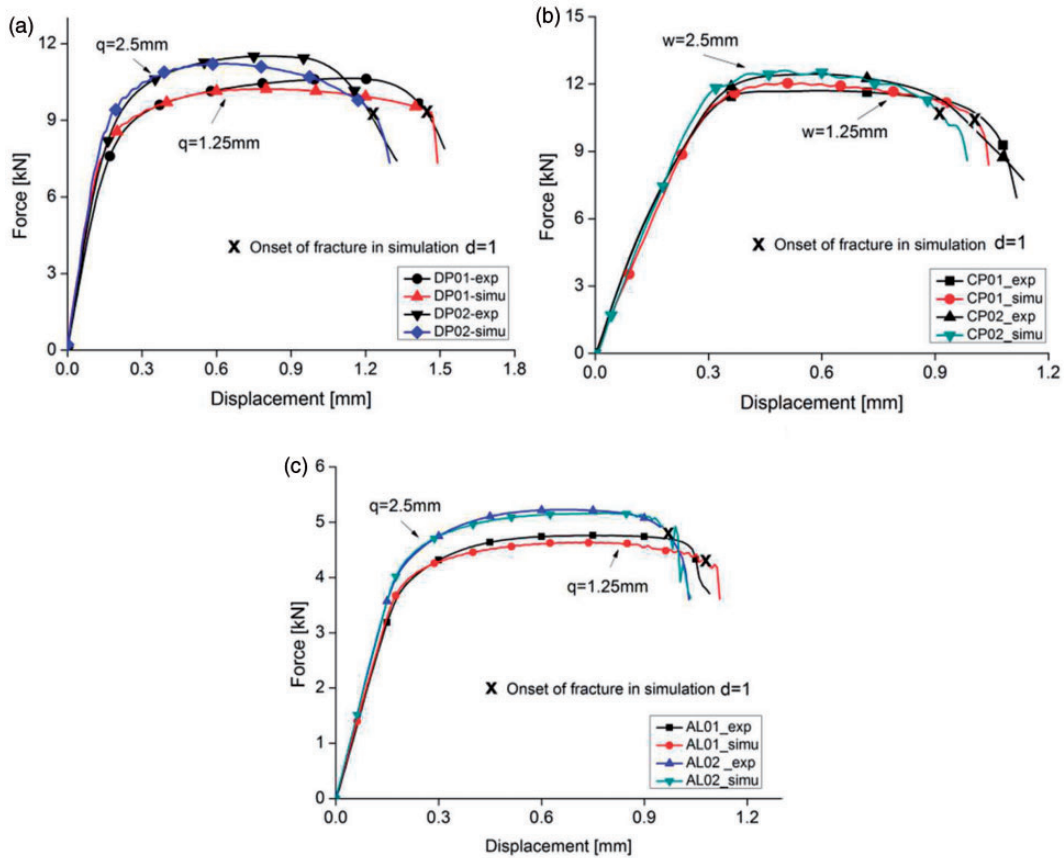


Figure 14. Numerical and experimental responses comparison of SS tests with different band angles.

Thus, according to this experience, 3D element is recommended to be the best choice for the damage prediction simulation in future.

Validation using additional tests

In order to validate the identified results, the additional tests (SS tests with $q = 1.25$ and 2.5 mm) are conducted and the geometries are shown in Figure 3(b). Based on the shear test specimen, the length of the connecting band is constant, and change the angle between band direction and loading direction, a combined shear and tension loading state is performed in the band region. This geometry is simulated to check the applicability of the material parameters determined earlier, which also includes the microcracks closure determined by SS. The gap distance 1.25 and 2.5 mm is chosen, which can create various combined tension and shear stress state in the test zone, the final test results are shown in Figure 14.

From the comparison of the experimental–numerical responses of SS tests with $q = 1.25$ and 2.5 mm it can be seen that there is a good agreement between them including elastoplasticity parameters ($E, \nu, \sigma_y, F, G, H, L, M, N, C, a, Q, b$), damage parameters ($S, s, \beta, Y_0, D_c, \gamma$), microcracks closure

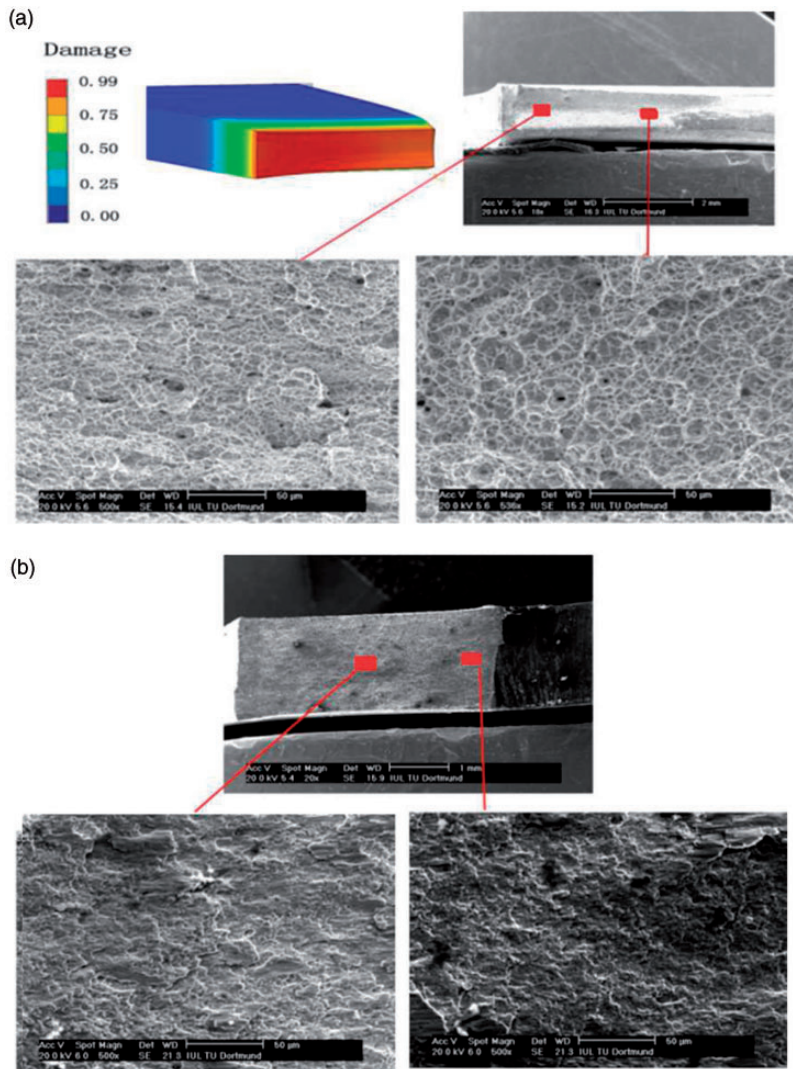


Figure 15. Micrograph showing the postmortern fracture surface: (a) notched specimen, (b) shear specimen.

(h), although there is no consistent maximum load for DP1000 between experiments and simulations in Figure 14(a). The problem has been found in Li et al. (2011). That can be explained by the influence of stress states on yield stress surface. The error ranges of the limit displacements between the simulations and experiments are limited in 5.0%, which can be regarded as the proof that the fully coupled model with the parameters determined with tests proposed in this study has accurately predicted the failure in the various combined shear and tension stress states of sheet metal forming.

Damage mechanism (scanning electron microscopy (SEM))

Ductile fracture governed by void growth and coalescence strongly depends on stress triaxiality (Gao and Kim, 2006; Gao et al., 2009; Zadpoor et al., 2009). In view of the micromechanics, the

final fracture phase is achieved by the link-void formation. This formation of the fracture can be divided into three modes: Mode I, II, and III. The ductile failure mechanism of mode I loading is well known. The modeling of this failure mechanism is also rather established (Gurson, 1977; McClintock, 1968; Rice and Tracey, 1969). During recent years this process is presented involving nucleation, growth, and coalescence of voids. This mechanism is induced by the high hydrostatic stress state and causes a dimple rupture. Here the final link up of the enlarged voids takes place by necking of the inter-void ligaments. In a mode II or III loading situation, the fracture is described by the shear stress state ahead of the crack tip which causes the shear localization, and stress state plays less important role in the fracture development. The formation can be named shear dimple rupture, which takes place by shearing of the inter-void ligaments (Barsoum and Faleskog, 2007).

In order to identify the fracture mechanism, we used the SEM to examine the fracture surface of DP1000. Figure 15 shows the damage contour on the fracture surface of the notched part. It is clear that the critical point of the damage is in the center of the necking part. This element first reaches the critical damage value and fails. In order to verify this conclusion, we used SEM to observe the surface of fracture. Figure 15(a) shows the microstructure of the fracture surface. The profile of the simulation also well fits with the real fracture surface, and from the pictures we can see many typical void-dimple structures on the surface which is the tensional failure (mode I). Normally, due to the higher density of microvoids and larger dimension, the size of the microvoids in the center of the necking part should be larger, that is in accordance with the observed result.

Figure 15(b) clearly shows the sheared or river marking fracture form in the center of the failure surface. By contrast with the microstructure the fracture shown in Figure 15(a) can be considered as typically mode II fracture. The feature on the edge of the surface can be considered as the combined normal and shear fracture, where rather flat dimple formations are observed on the fracture surface.

Conclusions

An involved methodology toward identification of the parameters pertaining to damage coupled anisotropic plasticity with kinematic and isotropic hardening and crack closure effects is presented. On the experimental side, in view of stress triaxiality effects on the ductile damage evolution, tests of UT, TBT, PNT, and SS are conducted which span a large interval of stress triaxiality ratios. The SS is explicitly used as a means to define crack closure parameter which requires at least one compressive tensile principal stresses. The optical device ARAMIS is used to measure the relative distance of the local node pairs on the specimens to eliminate the machine stiffness effects. A number of node pairs are observed to keep track of the size of the localization zone within the material. Using the possibility of isolated plasticity and damage concepts at relatively earlier deformation which relies on the physical facts, the combined kinematic and isotropic plasticity of the sheets are quantified through UT and TBR tests. An inverse optimization method, relying on the optical measurement results and the simulations, is developed to characterize the degeneration process of the sheets in different stress states with PNT and SS tests. The simulation responses coupled with identified damage parameters of SS ($q = 1.25$ and 2.5 mm) show good agreement with the experimental responses, which prove the applicability of the calibration process and validation of specified parameters. Finally, a qualitative analysis regarding the fracture modes for different tests and geometries is conducted through SEM observations. It is seen that the fracture morphologies are in accordance with the simulation results.

The main contribution of the present work is the combined experimental-numerical methodology proposed for the parameter identification. This methodology is tailored for the selected material model accounting for anisotropic plastic flow, mixed isotropic and kinematic hardening, and isotropic ductile damage with microcracks closure effect. Through the comparisons of simulations and experimental

responses, the present fully coupled CDM model shows good accuracy on the prediction of the cracks initiation under a wide range of simple stress states. In a coming work, further investigations using this fully coupled model applied to various materials subject to more complex loading paths will be performed.

Acknowledgements

The authors thank Dr Hosen Sulaiman for providing us with valuable comments and continuous support. The financial support of this work through the China scholarship council (CSC) is gratefully acknowledged.

Conflict of interest

None declared.

Funding

This research received no specific grant from any funding agency in the public, commercial, or not-for-profit sectors.

References

- Abel A and Ham RK (1966) The cyclic strain behavior of crystals of aluminum-4 wt.% copper—i. The Bauschinger effect. *Acta Metallurgica* 14: 1489–1494.
- Aravas N (1986) The analysis of void growth that leads to central burst during extrusion. *Journal of the Mechanics and Physics of Solids* 34: 55–79.
- ASTM (2000) D3039-00 Standard test method for tensile properties of polymer matrix composite materials. In: *Annual Book of ASTM Standards*, vol. 15, no. 03, ASTM International, West Conshohocken, USA.
- Badreddine H, Saanouni K and Dogui A (2010) On non-associative anisotropic finite plasticity fully coupled with isotropic ductile damage for metal forming. *International Journal of Plasticity* 26: 1541–1575.
- Badreddine H, Saanouni K and Nguyen TD (2014) Evolution of the plastic anisotropy induced by anisotropic damage under large plastic strains (submitted to International journal of solids and structures October 2013 to appear in 2014).
- Bai Y and Wierzbicki T (2008) A new model of metal plasticity and fracture with pressure and Lode dependence. *International Journal of Plasticity* 24: 1071–1096.
- Bao Y and Wierzbicki T (2004) A comparative study on various ductile crack formation criteria. *Journal of Engineering Materials Technology* 126: 314–324.
- Barsoum I and Faleskog J (2007) Rupture mechanisms in combined tension and shear experiments. *International Journal of Solids and Structures* 44: 1768–1786.
- Benzerger AA and Leblond JB (2010) Ductile fracture by void growth to coalescence. *Advances in Applied Mechanics* 44: 169–305.
- Besson J (2009) Damage of ductile materials deforming under multiple plastic or viscoplastic mechanisms. *International Journal of Plasticity* 25: 2204–2221.
- Besson J (2010) Continuum models of ductile fracture: A review. *International Journal of Damage Mechanics* 19: 3–52.
- Besson J, Steglich D and Brocks W (2003) Modeling of plan strain ductile rupture. *International Journal of Plasticity* 19: 1517–1541.
- Bonora N (1999) Identification and measurement of ductile damage parameters. *Journal of Strain Analysis for Engineering Design* 34: 463–478.
- Bonora N, Gentile D, Pironi A, et al. (2005) Ductile fracture evolution under triaxial state of stress: Theory and experiments. *International Journal of Plasticity* 21: 981–1007.
- Bouchard P-O, Gachet J-M and Roux E (2011) Ductile damage parameters identification for cold metal forming applications. In: Menary G (ed.) *The 14th international ESAFORM conference on material forming: ESAFORM 2011*, 27–29 April 2011, Belfast, UK. AIP Conference Proceedings, vol. 1353, pp. 47–52.
- Brokken D, Brekemans W and Baaijens F (1998) Numerical modeling of the metal blanking process. *Journal of Materials Processing Technology* 83: 192–199.

- Cao T-S, Gaillac A, Montmitonnet P, et al. (2013a) Identification methodology and comparison of phenomenological ductile damage models via hybrid numerical–experimental analysis of fracture experiments conducted on a zirconium alloy. *International Journal of Solids and Structures* 24: 3984–3999.
- Cao T-S, Gaillac A, Montmitonnet P, et al. (2013b) On the development and identification of phenomenological damage models—application to industrial wire drawing and rolling processes. *Key Engineering Materials* 554–557: 213.
- Celentano DJ and Chaboche JL (2007) Experimental and numerical characterization of damage evolution in steels. *International Journal of Plasticity* 23: 1739–1762.
- Chaboche J-L (1992) Damage induced anisotropy: On the difficulties associated with the active/passive unilateral condition. *International Journal of Damage Mechanics* 1: 148–171.
- Chaboche J-L (1993) Development of continuum damage mechanics for elastic solids sustaining anisotropic and unilateral damage. *International Journal of Damage Mechanics* 2: 311–329.
- Chow CL and Wang J (1987) An anisotropic theory of continuum damage mechanics for ductile fracture. *Engineering Fracture Mechanics* 27: 547–558.
- Daudeville L and Ladevèze P (1993) A damage mechanics tool for laminate delamination. *Composite Structures* 25: 547–555.
- Desmorat R, Gating F and Ragueneau F (2007) Nonlocal anisotropic damage model and related computational aspects for quasi-brittle materials. *Engineering Fracture Mechanics* 74: 1539–1560.
- Desmorat R, Gating F and Ragueneau F (2010) Nonstandard thermodynamics framework for robust computations with induced anisotropic damage. *International Journal of Damage Mechanics* 19: 53–73.
- Ebnoether F and Mohr D (2013) Predicting ductile fracture of low carbon steel sheets: Stress-based versus mixed stress/strain-based Mohr–Coulomb model. *International Journal of Solids and Structures* 50: 1055–1066.
- Eggertsen P-A and Mattiasson K (2010) An efficient inverse approach for material hardening parameter identification from a three-point bending test. *Engineering with Computers* 26: 159–170.
- Gao X and Kim J (2006) Modeling of ductile fracture: Significance of void coalescence. *International Journal of Solids and Structures* 43: 6277–6293.
- Gao X and Zhang G (2010) A study on the effect of the stress state on ductile fracture. *International Journal of Damage Mechanics* 19: 75–94.
- Gao X, Zhang T, Hayden M, et al. (2009) Effects of the stress state on plasticity and ductile failure of an aluminum 5083 alloy. *International Journal of Plasticity* 25: 2366–2382.
- Gelin JC (1990) Finite element analysis of ductile fracture and defects formations in cold and hot forging. *Annals of the CIRP* 39: 215–218.
- Gelin JC and Ghouati O (1994) An inverse method for determining viscoplastic properties of aluminum-alloys. *Journal of Materials Processing Technology* 45: 435–440.
- Gologanu M, Leblond J-B, Perrin G, et al. (1995) Recent extensions of Gurson's model for porous ductile metals. In: Suquet P (ed.) *Continuum Micromechanics*. New York, NY, USA: Springer-Verlag, pp. 61–130.
- Gurson AL (1977) Continuum theory of ductile rupture by void nucleation and growth: part I—yield criteria and flow rules for porous ductile media. *Journal of Engineering Materials and Technology* 99: 2–15.
- Hartley P, Clift SE, Salimi J, et al. (1989) The prediction of ductile fracture initiation in metal forming using a finite element method. *Research Mechanica* 28: 269–293.
- Johnson GR and Cook WH (1985) Fracture characteristics of three metals subjected to various strains, strain rates, temperatures and pressures. *Engineering Fracture Mechanics* 21: 31–48.
- Khoddam S, Lam YC and Thomson PF (1996) An inverse computational method for determining the constitutive parameters using the hot torsion test results. *Steel Research International* 67: 22–25.
- Lee H, Peng KE and Wang J (1985) An anisotropic damage criterion for deformation instability and its application to forming limit analysis of metal plates. *Engineering Fracture Mechanics* 21: 1031–1054.
- Lemaitre J (1992) *A Course on Damage Mechanics*. Berlin: Springer.
- Lemaitre J and Chaboche JL (1985) *Mécanique des matériaux solides*. Paris: Dunod.
- Lemaitre J, Chaboche JL, Benallal A, et al. (2009) *Mécanique des matériaux solides*, 3rd ed. Paris: Dunod.
- Lemaitre J and Desmorat R (2005) *Engineering Damage Mechanics*. Berlin, Germany: Springer.
- Li H, Fu MW, Lu J, et al. (2011) Ductile fracture: Experiments and computations. *International Journal of Plasticity* 27: 147–180.

- Li SX and Smith DJ (1998) Development of an anisotropic constitutive model for single crystal super alloy for combined fatigue and creep loading. *International Journal of Mechanical Sciences* 40: 937–938.
- McClintock FA (1968) A criterion for ductile fracture by the growth of holes. *Journal of Applied Mechanics* 35: 363–371.
- Marigo JJ (1985) Modeling of brittle and fatigue damage for elastic materials by growth of microvoids. *Engineering Fracture Mechanics* 21: 861–874.
- Merklein M and Biasutti M (2011) Forward and reverse simple shear test experiments for material modeling in forming simulations. In: *Steel research international, Special edition: 10th international conference on technology of plasticity*. Aachen, Germany, vol. 1, pp. 702–707.
- Murakami S (2012) *Continuum Damage Mechanics: A Continuum Mechanics Approach to the Analysis of Damage and Fracture*. Dordrecht: Springer-Verlag.
- Needleman A and Triantafyllidis N (1980) Void growth and local necking in biaxially stretched sheets. *Journal of Engineering Materials and Technology* 100: 164–172.
- Onate E and Kleiber M (1988) Plastic and viscoplastic flow of void containing metal—applications to axisymmetric sheet forming problem. *International Journal for Numerical Methods in Engineering* 25: 237–251.
- Ortiz M (1985) A constitutive theory for inelastic behavior of concrete. *Mechanics of Materials* 4: 67–93.
- Pardoen T, Hachez F, Marchioni B, et al. (2004) Mode I fracture of sheet metal. *Journal of the Mechanics and Physics of Solids* 52: 423–452.
- Qi W and Bertram A (1999) Anisotropic continuum damage modeling for single crystals at high temperatures. *International Journal of Plasticity* 15: 1197–1215.
- Rice JR and Tracey DM (1969) On the ductile enlargement of voids in triaxial stress fields. *Journal of the Mechanics and Physics of Solids* 17: 201–217.
- Rousselier G (1987) Ductile fracture models and their potential in local approach of fracture. *Nuclear Engineering and Design* 105: 97–111.
- Rousselier G (2001) Dissipation in porous metal plasticity and ductile fracture. *Journal of the Mechanics and Physics of Solids* 49: 1727–1746.
- Saanouni K (2012) *Damage Mechanics in Metal Forming: Advanced Modeling and Numerical Simulation*. London: ISTE Ltd; Hoboken, NJ: John Wiley & Sons.
- Saanouni K and Chaboche JL (2003) Computational damage mechanics. Application to metal forming. In: Milne I, Ritchie RO and Karihaloo B (eds) *Numerical and Computational Methods*. Oxford, UK: Elsevier, Chapter 7 of Vol. 3, pp. 321–376.
- Saanouni K, Forster Ch and Ben Hatira F (1994) On the anelastic flow with damage. *Engineering Damage Mechanics* 3: 140–169.
- Saanouni K and Hammi Y (2000) Numerical simulation of damage in metal forming processes, Continuous Damage and Fracture. In: Benallal A (ed.) *Continuous Damage and Fracture*. Elsevier, pp. 353–363.
- Saanouni K, Lestriez P and Labergère C (2011) 2D adaptive simulations in finite thermo-elasto-viscoplasticity with ductile damage: Application to orthogonal metal cutting by chip formation and breaking. *International Journal of Damage Mechanics* 20: 23–61.
- Shouler DR and Allwood JM (2010) Design and use of a novel sample design for formability testing in pure shear. *Journal of Materials Processing Technology* 210: 1304–1313.
- Simo JC and Ju JW (1987) Strain and stress based continuum damage models. *International Journal of Solids and Structures* 23: 821–869.
- Soyarslan C and Tekkaya AE (2010) A damage coupled orthotropic finite plasticity model for sheet metal forming: CDM approach. *Computational Materials Science* 48: 150–165.
- Soyarslan C, Tekkaya AE and Akyuz U (2008) Application of continuum damage mechanics in discontinuous crack formation: Forward extrusion chevron predictions. *Journal of Applied Mathematics and Mechanics* 88: 436–453.
- Tvergaard V (1990) Material failure by void growth to coalescence. *Advances in Applied Mechanics* 27: 83–147.
- Unger J, Stierner M, Brosius A, et al. (2008) Inverse error propagation and model identification for coupled dynamic problems with application to electromagnetic metal forming. *International Journal of Solids and Structures* 45: 442–459.
- Voyiadjis GZ and Kattan PI (1992) A plasticity-damage theory for large deformations of solids. Part I: Theoretical formulation. *International Journal of Engineering Science* 30: 1089–1108.

- Xue L (2007) Damage accumulation and fracture initiation in uncracked ductile solids subject to triaxial loading. *International Journal of Solids and Structures* 44: 5163–5181.
- Yin Q, Soyarslan C, Güner A, et al. (2012) A cyclic twin bridge shear test for the identification of kinematic hardening parameters. *International Journal of Mechanical Sciences* 59: 31–43.
- Yoshida F, Urabe M, Hino R, et al. (2003) Inverse approach to identification of material parameters of cyclic elasto-plasticity for component layers of a bimetallic sheet. *International Journal of Plasticity* 19: 2149–2170.
- Yoshida F, Urabe M and Toropov VV (1998) Identification of material parameters in constitutive model for sheet metals from cyclic bending tests. *International Journal of Mechanical Sciences* 40: 237–249.
- Yoshida Y and Ishikawa T (2011) Determination of ductile damage parameters by notched plate tensile test using image analysis. *Materials Research Innovations* 15: 422–425.
- Zadpoor AA, Sinke J and Benedictus R (2009) Formability prediction of high strength aluminum sheets. *International Journal of Plasticity* 25: 2269–2297.
- Zhu YY, Cescotto S and Habraken AM (1992) A fully coupled elastoplastic damage modeling and fracture criteria in metal forming processes. *Journal of Materials Processing Technology* 32: 197–204.

Appendix I. About the used inverse approach

The hybrid experimental–numerical methodology used in this paper belongs to the inverse approach category, where certain input data are deduced from the comparison between the experimental results and numerical simulation results. Here, the relevant information from experiments can be the displacement–load responses or full-field surface measurements with optical measurement system. The inverse method here is narrowed to the optimization of the material parameters including hardening parameters and damage parameters. The basic principle of inverse methodology is almost the same, which is to search the minimum error value between simulation and experiment responses

$$g(x_i) = \frac{1}{N} \sum_{n=1}^N W_n \left(\frac{f_n(x_i) - F_n(x_i)}{Z_{area}} \right)^2 \quad (20)$$

where $g(x_i)$ is the objective function expressed in terms of weighted least square form, x_i is the parameter needed to be optimized, N denotes the total number of observations (sample points), $f_n(x_i)$ is the simulation force response, $F_n(x_i)$ is the objective experimental response, $Z_{area} = \sigma_y \varpi$ is residual scale factor, ϖ denotes the size of loading cross section surface, W_n is the weighting factors, equal to $1/N$ here, which means the even weighting factors. For damage parameter identification, six experimental data in the form of force–point displacement related to local 1.0 and 4.0 mm away from the notched axis of three PNT tests are proposed to identify the damage parameters (S, s, β), so N value, here is 6.

In this study, in order to minimize the objective function, the trust region reflective method is used, which suits itself to nonlinear least square optimization problem. The optimization process involves the approximate solution of a large linear system based on the method of preconditioned conjugate gradients. The identification procedure requires the definition of bounds for each parameter, namely x_i^{min} , x_i^{max} . With the help of the normalized function ξ_i^n (its bound should be in (0, 1)), the actual value for each unknown parameter can be created, as shown below

$$x_i^{n+1} = x_i^{min} + (x_i^{max} - x_i^{min}) \cdot \xi_i^{n+1} \quad (21)$$

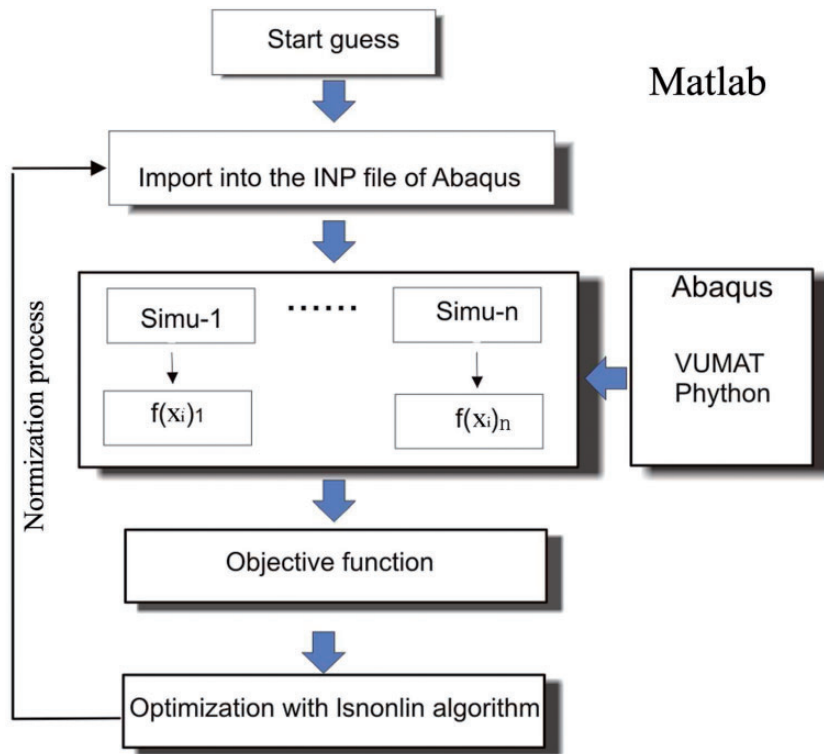


Figure 16. Flow chart of inverse optimization process.

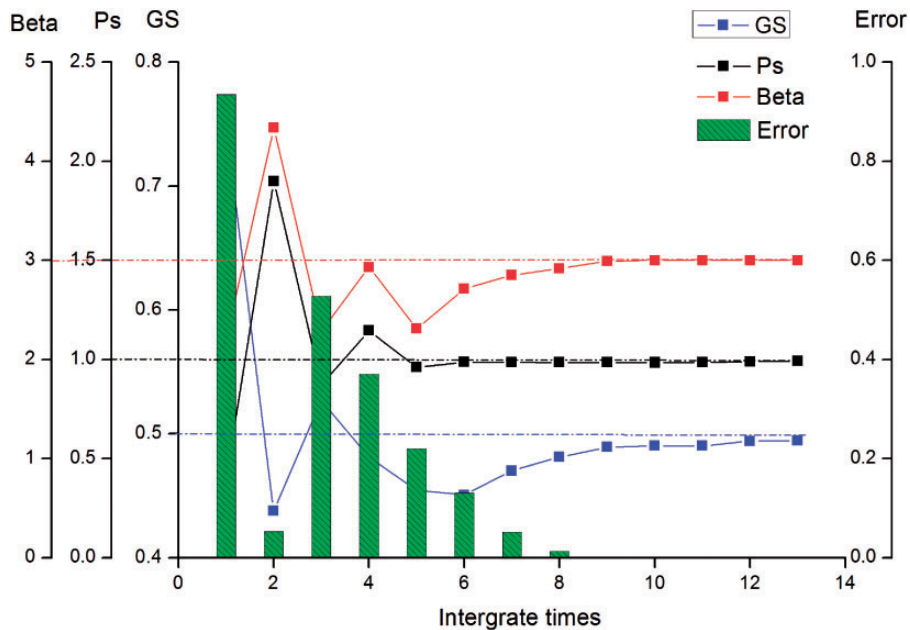


Figure 17. The parameters convergence process with initial set of $(S, s, \beta) = (0.75, 0.4, 2.2)$.

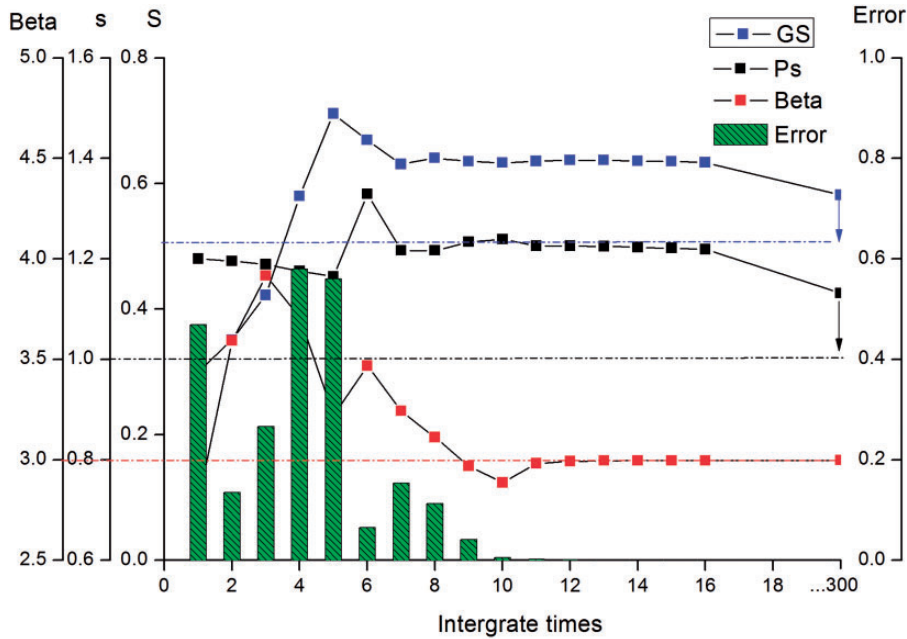


Figure 18. The parameters convergence process with initial set of $(S, s, \beta) = (0.3, 1.2, 2.8)$.

The global criteria of the convergence are that the numerical results must satisfy the following conditions

$$g(x_i) < \theta_{total} \quad (22)$$

where θ_{total} is the limit tolerance between the simulation and experiment force.

The whole optimization process works based on a set of MATLAB code which is written linking ABAQUS/Explicit solver. With ABAQUS script language python, the objective data can be read from the objective file. The optimization process can be divided in six stages, which include: operate the ABAQUS simulation, read global data, compare the results with the experimental measurements, build and minimize the objective function, optimize parameters, and update the input file. The detail of the optimization process is shown in Figure 16. The verification of the developed optimization scheme is given below.

The verification study depends on uniaxial tension of a single finite element which is free of the mesh size effects. The analytical expression for the damage development for this stress state is given in equation (23). Initially, the test is run for a known parameter set of $E = 200,000$ MPa and $\nu = 0.3$, $\sigma_y = 900$ MPa, $K = 100$, and (S, s, β) as $(0.5, 1.0, 3.0)$ and the response is recorded, the (x_i^{min}, x_i^{max}) here are chosen to be $(0-1, 0-3, 0-5)$ for (S, s, β) with empirical assumption. Then, the target damage parameters can be identified with different sets of initial values

$$D = 1 - \left[1 - \left(\frac{1+\nu}{3ES} \right)^s \frac{\beta+1}{(2s+1)K} \left[(\sigma_y + K\alpha)^{2s+1} - \sigma_y^{2s+1} \right] \right]^{\frac{1}{\beta+1}} \quad (23)$$

In order to show the importance of initial value for the convergence, two comparable examples with different initial set of values are given. The convergence pattern with initial set of $(S, s, \beta) = (0.75, 0.4, 2.2)$ is given in Figure 17. As it is seen, the scheme locates the optimum value after 14 iterations. The situation for initial set of $(S, s, \beta) = (0.3, 1.2, 2.8)$ is shown in Figure 18. It can be found that after 300 iterations the final parameter set comes to $(0.55, 1.5, 3)$ and arrives at the optimum value after more than 1000 iterations, but it can be seen that the error between the experimental numerical results can be negligible (less than 1%) compared with initial error after 10 iterations, so this inverse method is applicable for the parameter identification.